

Segregation to  $\alpha_2/\gamma$  interfaces in TiAl alloys: A multiscale QM/MM studyD. Gehringer,<sup>1,\*</sup> L. Huber,<sup>2,†</sup> J. Neugebauer<sup>1,‡</sup> and D. Holec<sup>1,§</sup><sup>1</sup>Department of Materials Science, Montanuniversität Leoben, Franz-Josef-Straße 18, A-8700 Leoben, Austria<sup>2</sup>Max-Planck-Institut für Eisenforschung GmbH, Max-Planck-Straße 1, 40237 Düsseldorf, Germany

(Received 9 January 2023; accepted 27 April 2023; published 23 June 2023)

In this study we present an implementation of a coupled multiscale quantum mechanics/molecular mechanics approach well suited for studying compositionally rich extended defects. Our focus is on interfacial phenomena of  $\alpha_2/\gamma$  phase boundaries in intermetallic TiAl alloys. We prove that our implementation is capable of accurately reproducing site-preference energies of solutes reported by previous density functional theory studies. To properly study segregation phenomena, we developed a formalism for segregation energies in systems with two sublattices (Ti and Al). Our model provides predictions consistent with atom probe tomography measurements reported in literature for a large number of solute atoms.

DOI: [10.1103/PhysRevMaterials.7.063604](https://doi.org/10.1103/PhysRevMaterials.7.063604)

## I. INTRODUCTION

Extended defects, such as grain or phase boundaries have always been challenging for atomistic modeling. On the one hand, classical approaches such as molecular mechanics (MM), including both molecular statics and molecular dynamics, are capable of treating models with millions of atoms, and thus are an ideal tool for describing extended defects. However, they impose strong compositional limitations as interatomic potentials are available only for a limited number of systems. On the other hand, fully quantum-mechanical (QM) calculations, allowing a great deal of freedom with respect to the chemical compositions and crystal structures, constrain the model system size severely due to their computationally demanding nature.

A very promising solution to this obstacle seem to be approaches employing the fast-emerging machine-learned (ML) potentials [1], recently including also on-the-fly optimization [2]. Despite their great promise, they are not suitable for scanning over a large variety of compositions, such as high-throughput characterization of alloying impact. A single potential covering all alloying elements is difficult, if not impossible, to be optimized, while the generation of many very focused potentials for each species may be computationally prohibitive.

An alternative to ML potentials is a multimethod hybrid QM/MM scheme combining advantages of both, MM (or ML

potentials [3]) and QM (compositional freedom) methods, in spatially separated regions. Using ML potentials, that capture elastic properties of the material well in the MM region, can simplify the coupling process (see Sec. IID) significantly, compared to standard potentials. Although it has been around for decades, applying the QM/MM method to metallic systems is not trivial due to the delocalized electrons involved in their metallic bonding. Nevertheless, coupling of the atomistic and quantum-mechanical methods for metallic systems underwent important developments in recent years [4–8]. In the present study, we follow the strategy suggested by Huber *et al.* [8] and apply it to investigate the alloying impact on segregation and mechanical properties of phase boundaries.

We have selected the TiAl intermetallic system for this case study. Our motivation is threefold. Firstly, the base TiAl system is simple enough (simple crystallographic structures, non-magnetic, binary, stable,...) to allow for testing new methodological implementations. Specifically, we apply the QM/MM approach to study segregation to  $\text{Ti}_3\text{Al}/\text{TiAl } \alpha_2(1000)/\gamma(111)$  phase boundary. Secondly, the TiAl-based alloys have been extensively investigated (primarily experimentally), including numerous contributions from the Leoben group [9,10], thus guaranteeing sufficient data for validation of our predictions. Lastly, the development of novel TiAl-based alloys is a very vivid research area, both from the fundamental as well as from the applied (industrial) point of view. Therefore, consistent and complete data sets are necessary for the knowledge-based design of new systems.

To properly elucidate the behavior of solutes at a phase boundary, it is necessary to formulate the segregation energetics for a two-component two-phase system carefully. We present such an approach in Sec. III. The majority of the available literature deals with segregation in simple metals (e.g., Mg [11], Mo or W [12]).

The present paper is organized as follows: We first introduce structural models for the considered boundaries and the QM/MM methodology. Next, we focus on important aspects of coupled QM and MM calculations. Afterward, we

\* dominik.gehringer@unileoben.ac.at

† liamhuber@greyhavensolutions.com

‡ neugebauer@mpie.de

§ david.holec@unileoben.ac.at

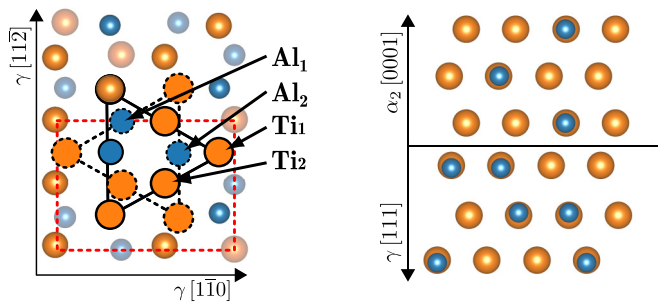


FIG. 1. Top view of the  $\alpha_2/\gamma$  interface (the  $\gamma$  half-crystal is rotated by  $180^\circ$ ). Translucent and dashed-bordered atoms belong to the bottom  $\gamma$  grain. The solid border atoms refer to the  $\alpha_2$  grain sitting above. The orange and blue spheres represent Ti and Al atoms, respectively.

compare two different QM/MM setups by benchmarking them against pure density functional theory (DFT) calculations. In the next section, we provide details for the discussion of the site preference and compare our results against literature data. The largest portion of the results focuses on determining the segregation and phase preference for selected  $3d$ ,  $4d$ , and  $5d$  transition metal solutes, and comparing the predictions with concentration profiles across phase boundaries determined using the atom probe tomography.

## II. COMPUTATIONAL METHODS

### A. Structural models for the interfaces

An advantage of the coherent phase boundary is that due to the periodic boundary conditions, the simulation cells can be small in the  $x$  and  $y$  (in-plane) directions. Our cells are aperiodic out-of-plane. As Kanani *et al.* pointed out, there is no unique way to model  $\alpha_2/\gamma$  interfaces [13,14], since the constituting half-crystals may be rotated against each other, thus making up different phase boundaries, yielding different interface energies. Based on their results we chose the energetically most favorable interface configurations [13,14], which are depicted in Fig. 1.

Although the  $\alpha_2(0001)/\gamma(111)$  interface yields a near-hexagonal cell, we have used orthogonalized cells. This is because the large-scale atomic/molecular massively parallel simulator's (LAMMPS's) triclinic crystal symmetry setting cannot handle hcp-like cells. Thereby, the number of atoms is doubled, which is particularly important for the QM region. Moreover, this reduces the relative solute concentration at the interface, which is  $1/16 = 6.25$  at.%. Each QM/MM cell consists of 56 layers, where each of those consists of eight atoms ( $56 \times 8 = 448$ ). The cells  $(\alpha_2(0001)/\gamma(111))$  contain 28 layers above and below the interface. The cell dimensions are  $5.77\text{\AA} \times 9.90\text{\AA} \times 130.02\text{\AA}$ . The cells are periodic along  $a$ , and  $b$  vectors and exhibit no periodicity along the  $c$  direction. Similarly, we constructed  $\alpha_2$  and  $\gamma$ -bulk cells to compute bulk formation energies, resulting in the same amount of atoms. We have chosen two QM/MM setups, which drastically differ in their computational demand. In the first (demanding) one, the model sizes were chosen such that the QM region results in similar (same number of atoms)

models as used in the previous work [15]. In the truly dilute limit, the planar cell dimensions should be much larger, however the above-mentioned in-plane dimensions make parts of the present study comparable with previous work and hence allows for validation of the new implementation. The computational cost of the demanding QM/MM setup is almost equal to the DFT. The overhead introduced in terms of CPU time due to QM/MM is (within this study) compared to the DFT setup on average less than one percent. The second setup is minimalistic and reduces the computational effort for a single-point calculation by roughly one order of magnitude. Finally, we repeat all calculations with DFT and benchmark both QM/MM setups against pure DFT. We show that QM/MM is also applicable to systems that are chemically more complex than simple metals.

### B. QM calculations

All quantum-mechanical calculations were carried out in the framework of DFT with the Vienna *ab initio* simulation package (VASP) [16,17]. The exchange and correlation functional was treated at a generalized gradient approximation level parametrized by Perdew-Burke-Ernzerhof [18,19]. For the electronic self-consistent cycle we set a convergence criterion of  $\Delta E_{SCF} = 10^{-4}$  eV. The convergence criterion for the ionic loop is discussed in Sec. II E. All calculations were carried out in non-spin-polarized mode. The projector augmented wave method [20,21] was used to describe the electron-ion interactions. The plane-wave cutoff energy was set to 350 eV. For the  $k$ -mesh sampling of the Brillouin zone, a Monkhorst-Pack [22] scheme with  $6 \times 3 \times 1$   $k$  points was chosen. These settings were used for the QM region of the coupled QM/MM calculations (Sec. II E). In DFT calculations carried out for benchmarking the QM/MM setups, we allow all ions to relax.

### C. MM calculations

MM calculations were performed with the LAMMPS simulator [23,24] using an embedded-atom-method (EAM) potential for the binary Al-Ti system parameterized by Zope and Mishin [25]. To make it compatible with the QM calculations, it was spatially rescaled to match the DFT computed lattice parameters of both  $\gamma$ -TiAl and  $\alpha_2$ -Ti<sub>3</sub>Al. This process is described in the next section.

### D. EAM potential rescaling

To obtain a force convergence during the coupled QM/MM relaxation, both methods [DFT and MM] should yield the same lattice parameters for the same phases. This rescaling is an important part of any QM/MM [6,26,27] scheme and has been extensively discussed by Huber *et al.* [8]. Therefore we calculated the potential energy surfaces (PES) for the unit cells of both phases,  $\gamma$ -TiAl (tetragonal) and  $\alpha_2$ -Ti<sub>3</sub>Al (hexagonal), as functions of the lattice parameters  $a$  and  $c$ ,  $E_{\text{DFT}}^\gamma(a, c)$  and  $E_{\text{DFT}}^{\alpha_2}(a, c)$ . The DFT-optimized lattice parameters corresponding to the global minimum on these PES are displayed in Table I. EAM potentials are tabulated on an equidistant mesh of radial points and the spatial distance  $\Delta r$  of the table entries is given in the potential header. We, therefore, computed the

TABLE I. Ground state lattice parameters produced by the rescaled EAM potential compared with DFT with settings described in Sec. II B.

	$\gamma$ -TiAl		$\alpha_2$ -Ti <sub>3</sub> Al	
	$a$	$c$	$a$	$c$
DFT [ $\text{\AA}$ ]	3.993	4.065	5.751	4.655
EAM [ $\text{\AA}$ ]	4.037	4.109	5.812	4.706
Deviation [%]	+1.11	+1.08	+1.08	+1.08
Rescaled EAM [ $\text{\AA}$ ]	3.995	4.065	5.749	4.654
Deviation [%]	+0.041	+0.011	-0.034	-0.025

$\Delta r$  value which minimises the objective function

$$(a_{\text{DFT}}^\gamma - a_{\text{MM}}^\gamma)^2 + (a_{\text{DFT}}^{\alpha_2} - a_{\text{MM}}^{\alpha_2})^2 + (c_{\text{DFT}}^\gamma - c_{\text{MM}}^\gamma)^2 + (c_{\text{DFT}}^{\alpha_2} - c_{\text{MM}}^{\alpha_2})^2 \quad (1)$$

The equilibrium lattice parameters of the rescaled EAM potential, as well as their deviations from the DFT values, are shown in Table I.

Table I shows that the rescaled EAM potential largely reduces the deviation between DFT and MM. Therefore, the aforementioned  $\Delta r$  was changed by  $\approx -0.98\%$ , such that the potential minimizes Eq. (1). Huber *et al.* [8] intensively assessed the influence of the lattice mismatch and number of buffer shells on the formation energies of solutes at a grain boundary. They show that a mismatch in bulk moduli between DFT and rescaled EAM potential does not lead to a substantial error [8,27]. Hence, we focused the rescaling solely on matching the lattice parameters. Nevertheless, there still exists a mismatch, which might cause an error introduced by the presented methodology. We will show in Sec. IV A that those differences are small ( $|E^{\text{DFT}} - E^{\text{QM/MM}}| < 10$  meV). Finally, we note that throughout the study we use only the rescaled EAM potential in the MM region.

### E. The QM/MM coupling

In a hybrid QM/MM approach the system is decomposed into two regions (I and II). Region one (I) is treated accurately with QM and is furthermore the domain where the solutes are placed. In the present study, we refer to those layers around the interface as the *core* region. The remaining part of the cell is treated with MM and is usually denoted as region II. In other words region I denotes the QM and II the MM part. We have used a QM/MM scheme as proposed by Huber *et al.* [27,8], to perform DFT/MD coupled relaxations. The algorithm was implemented in the `pyiron_contrib` [28] project within the `pyiron` framework [29]. The QM/MM workflow was implemented as a directed graph. For its visualization, the reader is referred to the Appendix C.

We have chosen two different QM/MM setups. For both setups, the *filler* region was chosen to be a second  $\alpha_2(0001)/\gamma(111)$  interface. The reason is that a material-material interface in contrast to a material-vacuum interface introduces only weak electronic perturbations, and therefore leads to accurate forces in the *core* region [8]. The first,

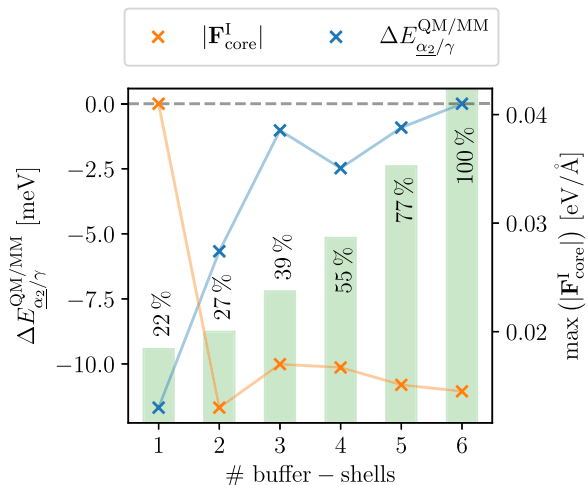


FIG. 2. Error estimation of the total QM/MM energy,  $\Delta E_{\alpha_2/\gamma}^{\text{QM/MM}}$ , (blue) and the maximum force norm on an atom in the *core* region of the QM cell,  $\max(|\mathbf{F}_{\text{core}}^{\text{I}}|)$  (orange) for a Pd decorated  $\alpha_2/\gamma$  interface as a function of buffer shells. The number of core shells was set to two. The reference line (black dashes) corresponds to  $N_{\text{buffer}}^{\text{shell}} = 6$ . The green bars represent the relative computational cost.

accurate, setup (denoted with  $\uparrow$ ) uses two atomic layers around the interface planes (the region of interest) for the *core* region. Furthermore, to obtain accurate total QM/MM energies and forces in the *core* region, we have chosen to construct six *buffer* layers to shield the *core* region. The convergence of the total energy as a function of the number of buffer shells, for a Pd decorated  $\alpha_2/\gamma$  interface is shown in Fig. 2. The same number of *core*, *buffer*, and *filler* layers were chosen for both  $\gamma$  and  $\alpha_2$ -bulk cells. Using this setup our QM region becomes similar to the cells used to study this system with pure DFT [15]. This setup yields 192 atoms in the QM region.

The second, minimalistic setup, in the following marked with  $\downarrow$ , uses only one *core* and one *buffer* shell and results in only 64 atoms in the QM region. This setting lowers the computational effort by roughly one order of magnitude.

All calculations are performed at constant volume obtained by optimizing the pristine cells with the EAM potential. The ionic positions of the coupled QM/MM systems were relaxed with a force convergence criterion  $\Delta F \leq 0.015$  eV/Å. To find the equilibrium positions, we used at most  $N_{\text{max}} = 200$  coupled steps with a gradient descent minimizer. The initial step size of the minimizer was set to  $\Gamma_0 = 0.075$ .

## III. EVALUATION METHODS

### A. Site preference

To determine the preferred sublattice  $\Theta$ , Al or Ti in our case, of a solute  $X$  in a bulk phase  $\mathbf{P}$ , we compare the formation energies of the solute of both sublattices. The formation energy reads

$$E_{\mathbf{P}}^{f,X \rightarrow \Theta} = E_{\mathbf{P}}^{X \rightarrow \Theta} - E_{\mathbf{P}} + \mu_{\mathbf{P}}^{\Theta} - \mu^X, \quad (2)$$

where  $E_{\mathbf{P}}^{X \rightarrow \Theta}$  denotes the energy where  $X$  replaces a  $\Theta$  atom.  $E_{\mathbf{P}}$  corresponds to the undecorated system. In bulk systems,  $\mu_{\mathbf{P}}^{\Theta}$  corresponds to a range of values rather than a single scalar.

Taking the difference of Eq. (2) for  $\Theta = \text{Ti}$  and  $\Theta = \text{Al}$ , eliminates the dependence of  $\mu_{\mathbf{P}}^X$  and yields

$$\begin{aligned}\Delta E_{\mathbf{P}}^{f,X} &= E_{\mathbf{P}}^{f,X \rightarrow \text{Al}} - E_{\mathbf{P}}^{f,X \rightarrow \text{Ti}} \\ &= E_{\mathbf{P}}^{X \rightarrow \text{Al}} - E_{\mathbf{P}} + \mu_{\mathbf{P}}^{\text{Al}} - \mu^X \\ &\quad - [E_{\mathbf{P}}^{X \rightarrow \text{Ti}} - E_{\mathbf{P}} + \mu_{\mathbf{P}}^{\text{Ti}} - \mu^X] \\ &= E_{\mathbf{P}}^{X \rightarrow \text{Al}} - E_{\mathbf{P}}^{X \rightarrow \text{Ti}} + \underbrace{\mu_{\mathbf{P}}^{\text{Al}} - \mu_{\mathbf{P}}^{\text{Ti}}}_{\Delta\mu_{\mathbf{P}}},\end{aligned}\quad (3)$$

which is solely a function of the difference of the chemical potentials  $\Delta\mu_{\mathbf{P}}$ . Hence, negative values of  $\Delta E_{\mathbf{P}}^{f,X}$  denote that  $X$  will prefer the Al sublattice. Consequently, the site preference of defects in the bulk system depends on the chemical potential difference  $\Delta\mu_{\mathbf{P}}$ , which is related to the composition. The range allowed for  $\Delta\mu_{\mathbf{P}}$  can be estimated by computing the thermodynamic limits, upon imposing the coexistence conditions with the neighboring phases. If  $\Delta E_{\mathbf{P}}^{f,X}$  does not cross the zero line within the thermodynamically accessible range of  $\Delta\mu_{\mathbf{P}}$ , we regard the alloying element  $X$  to exhibit a “strong” site preference in phase  $\mathbf{P}$ . Otherwise, we call it a “weak” or “compositionally dependent”. The actual values for the range of  $\Delta\mu_{\alpha_2}$  and  $\Delta\mu_{\gamma}$  are given in the next section, while for the derivation we refer the reader to Sec. A 1.

### B. Thermodynamic limits of the difference of chemical potentials

As  $\Delta\mu_{\mathbf{P}}$  is bounded by thermodynamic limits we have calculated those using Eqs. (A3)–(A6). For the stoichiometric composition,  $\Delta\tilde{\mu}_{\mathbf{P}}$  an expression is obtained by requiring the formation energies of the antisite defects to be identical. Therefore we get

$$E_{\mathbf{P}}^{f,\text{Ti} \rightarrow \text{Al}} \approx E_{\mathbf{P}}^{f,\text{Al} \rightarrow \text{Ti}}, \quad (4)$$

$$\Delta\tilde{\mu}_{\mathbf{P}} \equiv (\mu_{\mathbf{P}}^{\text{Ti}} - \mu_{\mathbf{P}}^{\text{Al}}) \approx \frac{E_{\mathbf{P}}^{\text{Al} \rightarrow \text{Ti}} - E_{\mathbf{P}}^{\text{Ti} \rightarrow \text{Al}}}{2}. \quad (5)$$

The  $\alpha_2$  phase ( $\mathbf{P} = \alpha_2$ ) is bordered by the  $\alpha$ -Ti with  $\approx 6$  at. % Al [30] for low and the  $\gamma$ -TiAl phase for high aluminum contents. Hence, we have computed the thermodynamic limits as  $-2.89 \text{ eV} = \Delta\mu_{\alpha/\alpha_2} \geq \Delta\mu_{\alpha_2} \geq \Delta\mu_{\alpha_2/\gamma} = -3.55 \text{ eV}$ . This is in good agreement with Wei *et al.* [15] who obtained  $-3.52 \text{ eV}$  for  $\Delta\mu_{\alpha_2/\gamma}$ . For the derivation of these limits, the reader is referred to Sec. A 1. For the difference at the stoichiometric composition we obtained  $\Delta\tilde{\mu}_{\alpha_2} = -3.30 \text{ eV}$ .

For the  $\gamma$ -TiAl phase, which borders  $h$ -TiAl<sub>2</sub> for high aluminum contents, we obtained for the limits  $-3.55 \text{ eV} = \Delta\mu_{\alpha_2/\gamma} \geq \Delta\mu_{\gamma} \geq \Delta\mu_{\gamma/h} = -3.96 \text{ eV}$  and  $\Delta\tilde{\mu}_{\gamma} = -3.71 \text{ eV}$  for the stoichiometric composition. The derivation is given in Sec. A 2.

### C. Segregation and phase-preference energies

Unlike in bulk regions of the  $\gamma$  and  $\alpha_2$  phases, where all Ti or Al sites are equivalent, breaking the translation symmetry at the interface may lead to various Ti or Al sites being nonequivalent. At a phase-boundary  $\mathbf{B}$ , on the atomistic level, each of the sublattices  $\Theta$  may split into  $i$  symmetry

inequivalent sites. For each of those sites for a solute  $X$  occupying this site the energy of formation reads

$$E_{\mathbf{B}}^{f,X \rightarrow \Theta_i} = E_{\mathbf{B}}^{X \rightarrow \Theta_i} - E_{\mathbf{B}} + \mu_{\mathbf{B}}^{\Theta} - \mu_{\mathbf{B}}^X. \quad (6)$$

Consequently, we refer to the minimal of those formation energies as the formation energy for a specific sublattice  $\Theta$  of a boundary  $\mathbf{B}$

$$E_{\mathbf{B}}^{f,X \rightarrow \Theta} = \min_i E_{\mathbf{B}}^{f,X \rightarrow \Theta_i}. \quad (7)$$

Indeed, at the  $\alpha_2/\gamma$  interface, a solute can be placed at two chemically distinct Ti sites on the  $\alpha_2$  side of the interface and at two different Al sites on the  $\gamma$  side. We distinguish those by a subscript index. Hence, similarly to Eq. (3), using Eq. (7) one can define the difference in the sublattice formation energies, to investigate site preference at the boundary.

Moreover, in the following, we distinguish between two scenarios. The solute  $X$  decorating the  $\alpha_2$  side we refer to as  $\alpha_2/\gamma$  and similarly  $\alpha_2/\gamma$  for  $X$  sitting on the opposite side. To elucidate the mechanisms at the  $\alpha_2/\gamma$  interface we define three differences of formation energies.

$$\begin{aligned}\Delta E_{\alpha_2 \rightarrow \alpha_2/\gamma}^f &= E_{\alpha_2/\gamma}^{f,X \rightarrow \Theta} - E_{\alpha_2}^{f,X \rightarrow \Theta'} \\ &= \min_{\Theta, \Theta' \in \{\text{Ti}, \text{Al}\}} [(E_{\alpha_2/\gamma}^{X \rightarrow \Theta_i} + E_{\alpha_2} + \mu^{\Theta}) \\ &\quad - (E_{\alpha_2}^{X \rightarrow \Theta'} + E_{\alpha_2/\gamma} + \mu^{\Theta'})],\end{aligned}\quad (8)$$

and similarly,

$$\Delta E_{\gamma \rightarrow \alpha_2/\gamma}^f = \min_{\Theta, \Theta' \in \{\text{Ti}, \text{Al}\}} E_{\alpha_2/\gamma}^{f,X \rightarrow \Theta} - E_{\gamma}^{f,X \rightarrow \Theta'}, \quad (9)$$

$$\Delta E_{\gamma \rightarrow \alpha_2}^f = \min_{\Theta, \Theta' \in \{\text{Ti}, \text{Al}\}} E_{\alpha_2}^{f,X \rightarrow \Theta} - E_{\gamma}^{f,X \rightarrow \Theta'}. \quad (10)$$

Note that in the case of  $\Theta = \Theta'$  the chemical potential terms vanish, otherwise they equate to  $\pm \Delta\mu_{\alpha_2/\gamma}$ . In contrast to the pure bulk setting, [Eq. (3)], the chemical potential  $\mu^{\Theta}$ , in Eqs. (8)–(10) becomes a single value. Due to the coexistence of the  $\alpha_2$  and  $\gamma$  phase, Gibbs’ phase rule yields one degree of freedom less. For Eqs. (8) and (9) a negative value corresponds to segregation to the interface at the corresponding site. In contrast, values for Eq. (10) represent a tendency for the solute  $X$  to partition into the  $\alpha_2$ -bulk phase. Figure 3 illustrates a schematic physical interpretation of the energies defined above for the  $\alpha_2/\gamma$  interface.

We note, that it is possible to come up with a single value for the segregation energy by minimizing the energy difference over all boundaries and bulk states simultaneously. Nevertheless, we think, the presented approach helps to elucidate the behavior of the solutes at the interface better, as it allows us to draw a qualitative spatial energy profile (see Fig. 3). As this concept, however, introduces some additional complexity, we have visualized Fig. 3 for each solute separately, where we used the  $\gamma$  bulk as a reference state in Fig. 8.

## IV. RESULTS AND DISCUSSION

### A. Benchmark QM/MM against DFT and literature

We have computed for 22 alloying elements the differences in the formation energies for the different sublattices [Eq. (3)] with DFT and compared it with our two QM/MM setups.

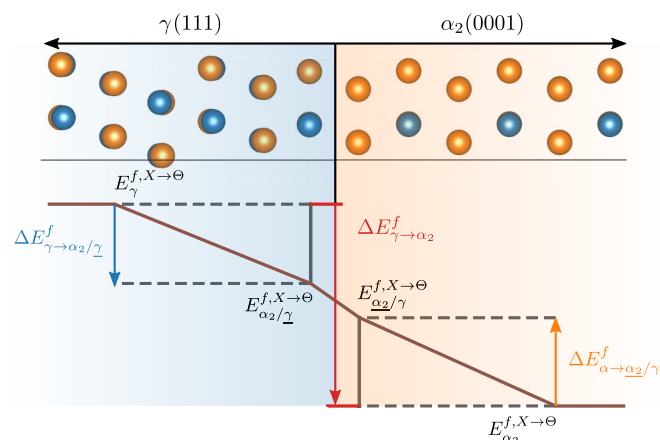


FIG. 3. Schematic illustration of the energy levels, and meaning of the defined energies at the  $\alpha_2(0001)/\gamma(111)$  interface. The brown line represents the spatial energy profile. The colored arrows correspond to the difference in formation energies. Eq. (9) – blue, Eq. (10) – red and Eq. (8) – orange.

Figure 4 shows the energy differences between the DFT and the QM/MM values for both setups. The green ribbon represents  $\pm 10$  meV and encloses all values of the “large” ( $\uparrow$  = squares) QM/MM setup. Thus it proves, that the difference between DFT and QM/MM is vanishing for demanding settings.

For the minimalistic QM/MM setup ( $\downarrow$ ), the differences are much larger, up to  $\approx 80$  meV for Pt. The deviations are larger in the  $\alpha_2$  phase, than in the  $\gamma$ -bulk phase. The difference tends to increase for later transition metals. This can be understood in terms of strain energy errors, which are introduced by the QM/MM methodology in two ways: first relaxations are only accounted for in the positional (and not cell) degrees of freedom, and second since the *filler* atoms are held fixed, large segregants may induce filler-buffer strain that does not cancel out in other components of the segregation energy calculation. The latter is of particular concern when the number of *core* shells is small. Nevertheless, usually  $\Delta E_P^f$  is in

the range of 1 eV, and consequently, even this setup produces very reasonable estimates, as we show later.

Figure 5 compares the values computed by Eq. (3) for the  $\alpha_2$  (upper panel) and  $\gamma$ -bulk phase (lower panel), for three different setups (DFT, QM/MM  $\uparrow$  and  $\downarrow$ ) to literature data. It, furthermore, confirms, as well as Fig. 4, that the presented QM/MM method is able to reproduce DFT extremely accurately. Secondly, even for minimalistic QM/MM settings ( $\downarrow$ ), our implementation manages to reproduce DFT values well. Although the differences might seem large in Fig. 4 at a first glance, they are small compared to the spread found throughout the presented literature data (see Table II).

Figure 5 reveals excellent agreement with the study of Wei *et al.* [15] for both  $\alpha_2$  and  $\gamma$  bulk phase. Comparing our data with Holec *et al.* [31] reveals a good agreement, yet a slight underestimation of  $\Delta E_{\alpha_2}^f$  and overestimation of  $\Delta E_{\gamma}^f$ . Furthermore, upon comparison with Benedek *et al.* [32], Fig. 5 reveals no systematic trend. Finally, the largest differences are observed, when comparing the present study with Ouadah *et al.* [33]. Interestingly, for the  $\alpha_2$  phase, there is a good agreement for Si and Cr, while for Cu, Nb, Mo, and Re the differences can be more than one hundred percent. ( $\Delta E_{\alpha_2}^f = 0.74$  eV compared to 1.58 eV for Re). A more detailed and quantitative analysis is presented in Table II.

Finally, in case the ranges shown in Fig. 5 are fully located in either the positive or negative regime, we refer (for bulk states) to as “strong” site preference, as the sublattice-formation energy cannot change its sign within the allowed regime. Otherwise, in the following we refer to as “weak” or “compositionally dependent” site preference.

Focusing on the decorated interfaces  $\alpha_2/\gamma$  and  $\alpha_2/\gamma$  yield similar results as for the bulk phases. Again, we find good agreement upon comparing our data with Wei *et al.* [15]. Similarly, the differences to Ouadah *et al.* [33] are rather large. For brevity, for the detailed plots similar to Fig. 5 for the decorated interfaces, we refer the reader to the Appendix B. Finally, comparing the differences between the three benchmark setups (DFT, QM/MM  $\uparrow$ , and QM/MM  $\downarrow$ ) are in the same

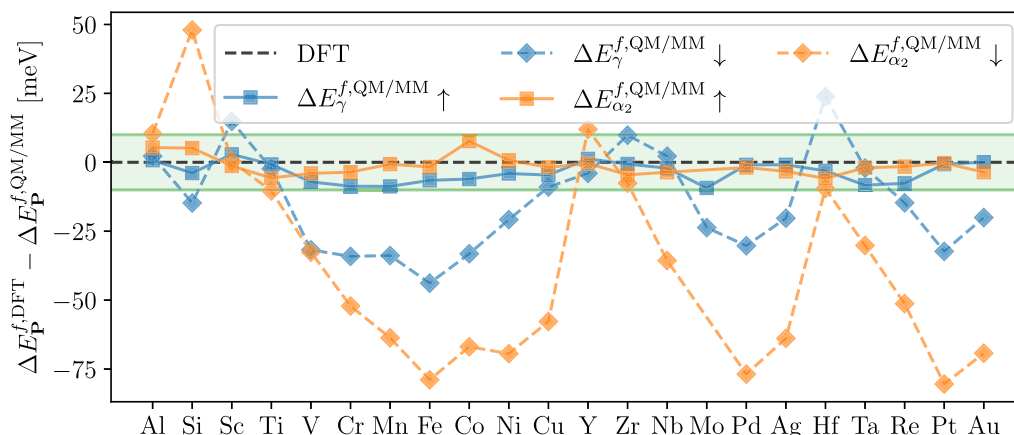


FIG. 4. Error in QM/MM computed formation energies [Eq. (3)] of different solutes in the  $\gamma$ -TiAl and  $\alpha_2$ -Ti<sub>3</sub>Al bulk, with respect to the full DFT reference. Squares represent the computationally more demanding QM/MM  $\uparrow$  and diamonds the minimalistic  $\downarrow$  setup. Orange refers to the  $\alpha_2$  and blue points to the  $\gamma$  phase. The green ribbon represents the target confidence interval of  $\pm 10$  meV region around the DFT reference.

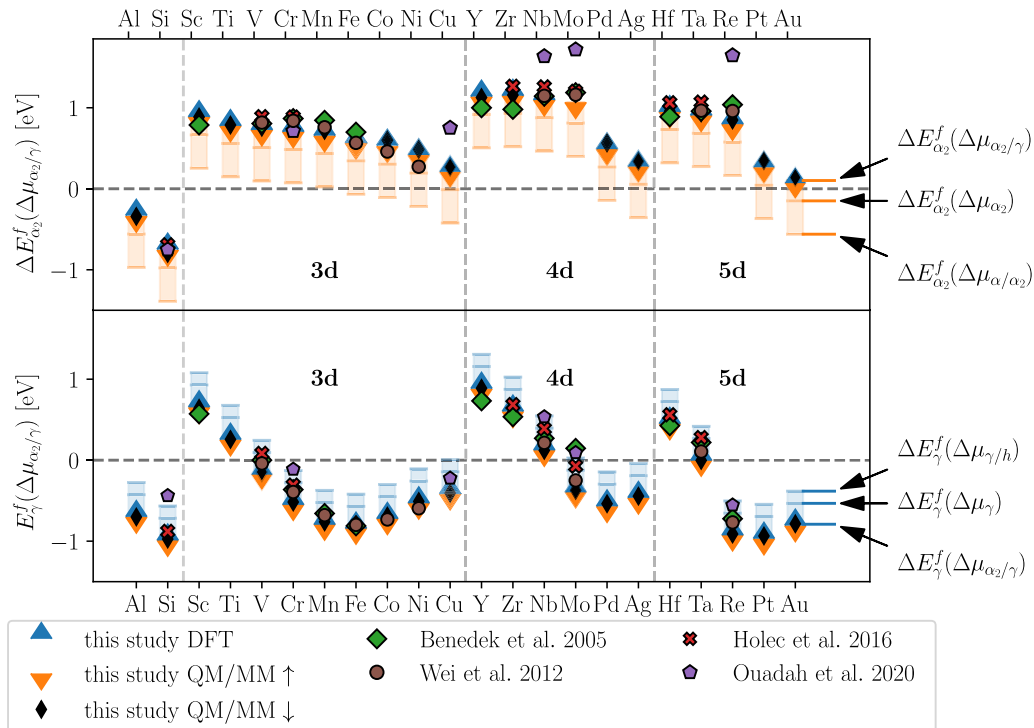


FIG. 5. Difference of the defect formation energy between [Eq. (3)] the Ti and Al sublattice for the  $\alpha_2$ -Ti<sub>3</sub>Al and the  $\gamma$ -TiAl bulk phases. The shaded regions represent the range of allowed values. The construction and meaning of the thermodynamic limits are defined in Sec. III B. Points, representing literature data, exhibit a small black border.

range as for the bulk models (Fig. 4), and hence negligible upon comparison to different DFT studies.

We conclude that the values obtained using the QM/MM method for bulk phases are in good agreement also with other older works for the  $\gamma$  phase [34–39] as well as for the  $\alpha_2$  phase [40]. Even for minimalistic a QM/MM setup ( $\downarrow$ ), deviations to the present DFT results are well below the spreads observed when compared to other studies.

### B. Site preference

We calculated the site-preference energies for a wide range of solutes for the  $\alpha_2$ - and  $\gamma$ -bulk phases as well as for the  $\alpha_2(0001)/\gamma(111)$  interface. For the  $\alpha_2(0001)/\gamma(111)$  interface we also have differentiated between the site-preference energy at each side of the interface,  $\alpha_2/\gamma$  and  $\alpha_2/\underline{\gamma}$ , respectively. For the bulk phases the  $\Delta E_{\mathbf{P}}^f$  is a function of  $\Delta\mu_{\mathbf{P}}$ , which allows drawing a point-defect phase diagram for each

of the solutes. For brevity, for these diagrams, we refer the reader to Appendix D. For the interface structure, this degree of freedom is lost due to the requirement of coexisting  $\alpha_2$  and  $\gamma$  phases. Therefore, in Fig. 6 we omit the thermodynamic limits.

#### 1. Site preference at the $\alpha_2(0001)/\gamma(111)$ interface

As mentioned in Sec. III A, there are two Ti sites at the  $\alpha_2$  side of the interface. The different sites are marked explicitly in Fig. 1. The first one (Ti<sub>1</sub>) exhibits five Al and seven Ti nearest neighbors. The Ti<sub>2</sub> site is surrounded by four Al and eight Ti atoms. Thus the Ti<sub>1</sub> is slightly Al rich compared with the Ti<sub>2</sub> site. The  $\gamma$  side of the interface also exhibits a splitting of the Al sublattice into two symmetry inequivalent sites. Al<sub>1</sub> sites have nine Ti and three Al neighbors (we refer to them as the Ti-rich sites), whereas Al<sub>2</sub> sites are surrounded by four Al and eight Ti atoms.

TABLE II. Average, standard and maximum deviation of the  $\Delta E_{\alpha_2}^f$  and  $\Delta E_{\gamma}^f$  compared to literature data, shown in Fig. 5. All values are in eV. The first column corresponds to the brown circles, the second to the red crosses, the third to the green square, and the fourth column to the purple pentagons in Fig. 5. The last column represents points denoted by the black diamonds.

$ \Delta E_{\mathbf{P}}^{f,\text{lit.}} - \Delta E_{\mathbf{P}}^f $		Wei [15]	Holec [31]	Benedek [32]	Ouadah [33]	QM/MM $\downarrow$
$\mathbf{P} = \alpha_2$	average	0.092	0.138	0.127	0.436	0.042
	std	0.048	0.038	0.058	0.323	0.027
	max	0.161	0.178	0.239	0.847	0.080
$\mathbf{P} = \gamma$	average	0.099	0.205	0.160	0.403	0.016
	std	0.045	0.085	0.128	0.111	0.011
	max	0.151	0.314	0.533	0.547	0.037

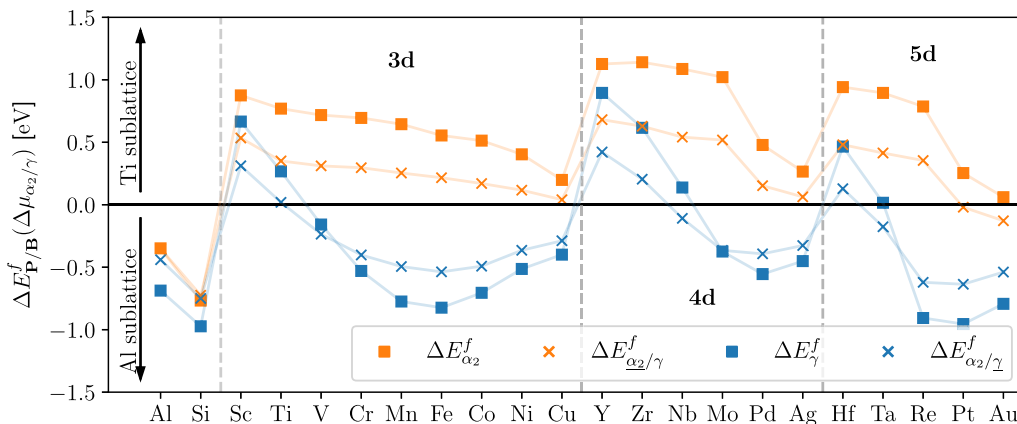


FIG. 6. Formation energy differences between Ti and Al sublattices. Orange squares represent  $\alpha_2$  bulk [Eq. (3)], crosses  $\alpha_2/\gamma$  boundary [Eq. (7)], blue squares  $\gamma$  bulk [Eq. (3)] and crosses  $\alpha_2/\gamma$  boundary [Eq. (7)]. All values are calculated at  $\Delta\mu_{\alpha_2/\gamma}$  (see Sec. III B).

Focusing on the latter ( $\gamma$ ) side, Table III reveals that Si and Al prefer the Ti-rich  $Al_1$  sites while all other solutes with the Al sublattice preference occupy the  $Al_2$  sites. Table III and Fig. 6 (blue) show that most of the solutes considered here prefer the Al site, and only the early 3d (Sc and Ti), 4d (Y and Zr) and (Hf and Ta) 5d elements prefer the Ti sublattice.

Absolute values of  $\Delta E_{\alpha_2}^f$  and  $\Delta E_{\alpha_2/\gamma}^f$  continuously decrease with increasing atomic number throughout the periods for the  $\alpha_2$  side of the interface (Fig. 6, orange diamonds). Our calculations predict that almost all transition metals prefer the Ti sites. Moreover, the Ti sublattice preference gets more pronounced with increasing period ( $3d < 4d < 5d$ ). Except for Sc, Zr, and Mn (preferring  $Ti_1$  sites), all elements prefer the  $Ti_2$  sites (Table III).

The early transition metals (Sc, Ti, Y, Zr, and Hf) prefer the Ti sublattice independent of the interface side. Except for V ( $\gamma$  side) and Cu and Pt ( $\alpha_2$  side), all elements preserve their bulk site preference, although the absolute values of the site energy at the interface decrease with respect to their bulk states (see arrows in Fig. 6). Thus, solutes become more “indifferent” about their preferred sublattice, most likely due to a less ordered chemical environment at the interface. This is in good agreement with previous works as mentioned in Sec. IV A.

### C. Segregation and phase-partitioning $E_{\gamma \rightarrow \alpha_2}^f$

The results are graphically summarized in Fig. 7. For a more detailed visualization, we refer the reader to Fig. 8.

Following the principle of minimum energy, the following segregation behavior is predicted:

#### 1. Partitioning into the $\gamma$ bulk phase.

Sc prefers both the  $\gamma$  side of the interface and the  $\gamma$  bulk over the  $\alpha_2$  side of the interface and the  $\alpha_2$  bulk phase. The positive values of  $E_{\gamma \rightarrow \alpha_2}^f$  further indicate that the bulk state is preferred (although marginally in the case of Sc).

#### 2. Partitioning into the $\alpha_2$ bulk phase.

3d transition metals (Cr, Mn, Fe, Co, Ni), as well as Mo, Pd, Ag, Ta, Au, Cu, and Re, prefer the  $\alpha_2$  phase. All those solutes show substantial positive (orange)  $E_{\alpha_2 \rightarrow \alpha_2/\gamma}^f$  values, and thus prefer the  $\alpha_2$  bulk state. Moreover, the elements show a strong phase preference for the  $\alpha_2$  bulk phase ( $E_{\gamma \rightarrow \alpha_2}^f < 0$ ).

#### 3. Elements segregating to the interface.

Y, V, Zr, and Nb exhibit the minimum energy state at the  $\gamma$  side of the interface. Y, Zr and Nb exhibit similar  $E_{\alpha_2 \rightarrow \alpha_2/\gamma}^f$  between  $-50$  and  $-100$  meV/at. Consequently, the preference for the interface (with respect to  $\gamma$  bulk) is rather small. Interestingly, the phase preference (and hence the driving force for segregation from the  $\alpha_2$  phase) is largest for Y and almost disappears for Nb. In contrast to those three elements, V shows a strong preference for the  $\gamma$  side of the interface state, although it otherwise prefers the  $\alpha_2$  bulk phase.

Si, Hf, and Pt are predicted to reside on the  $\alpha_2$  side of the interface. In the case of Si, this reflects the overall phase

TABLE III. Summary of the site-preference of different solutes, according to Eq. (2). Bold sublattice names indicate a strong site preference for the solute. When sublattice splitting occurs due to the broken symmetry at the interface, the preferred sites are indicated with subscript (see Sec. IV B 1 for an explanation).

	Al	Si	Sc	Ti	V	Cr	Mn	Fe	Co	Ni	Cu	Y	Zr	Nb	Mo	Pd	Ag	Hf	Ta	Re	Pt	Au
$\alpha_2$	<b>Al</b>	<b>Al</b>	Ti	<b>Ti</b>	Ti	Ti	Ti	Ti	Ti	Ti	Al	<b>Ti</b>	<b>Ti</b>	<b>Ti</b>	<b>Ti</b>	Ti	Ti	<b>Ti</b>	<b>Ti</b>	Ti	Ti	Al
$\gamma$	<b>Al</b>	<b>Al</b>	<b>Ti</b>	<b>Ti</b>	Al	<b>Al</b>	<b>Al</b>	<b>Al</b>	<b>Al</b>	<b>Al</b>	Al	<b>Ti</b>	<b>Ti</b>	<b>Ti</b>	Al	<b>Al</b>	<b>Al</b>	<b>Ti</b>	Ti	<b>Al</b>	<b>Al</b>	<b>Al</b>
$\alpha_2/\gamma$	Al	Al	$Ti_1$	$Ti_2$	$Ti_2$	$Ti_2$	$Ti_2$	$Ti_2$	$Ti_2$	$Ti_2$	$Ti_2$	$Ti_1$	$Ti_1$	$Ti_2$	$Ti_2$	$Ti_2$	$Ti_2$	$Ti_1$	$Ti_2$	$Ti_2$	Al	Al
$\alpha_2/\underline{\gamma}$	$Al_1$	$Al_1$	Ti	Ti	$Al_2$	$Al_2$	$Al_2$	$Al_2$	$Al_2$	$Al_2$	$Al_2$	Ti	Ti	Ti	$Al_2$	$Al_2$	$Al_2$	Ti	Ti	$Al_2$	$Al_2$	$Al_2$

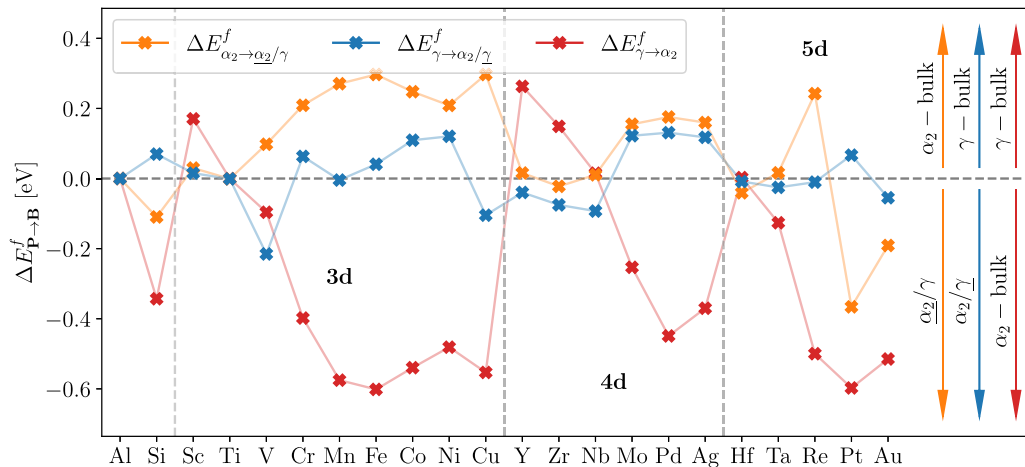


FIG. 7. Formation energy differences between interface and bulk for  $\alpha_2 \rightarrow \alpha_2/\gamma$  [orange, Eq. (8)] and  $\gamma \rightarrow \alpha_2/\gamma$  [blue, Eq. (9)]. Formation energy differences between both phases  $\gamma \rightarrow \alpha_2$ -bulk are shown in red, Eq. (10)

preference for the  $\alpha_2$  phase, and within that a slight preference for the interface position. A similar scenario applies also to Pt, whereby the preference for the interface is much stronger. Lastly, Hf exhibits a slight phase preference for the  $\gamma$  bulk phase, as well as negative segregation energy from both phases to the interface with the  $\alpha_2$  side being the preferred one.

#### 4. Comparison with experiments.

The amounts of alloying elements in experimentally studied alloys refer to the overall compositions and often range values above a few at. %. In multiphase systems, the alloying element is likely preferably present in one of the coexisting phases, whereas other phases are depleted of this element. Consequently, the local compositions may reach, e.g., above 10 at. %, and more. Enrichment at the phase boundary in the order 1 at. % is therefore difficult to detect, since in the same spacial region happens the transition from e.g., 10 at.% (phase containing the alloying element) to 0 at. % (phase depleted of the element). In other words, a strong phase preference may hinder the experimental observation of phase-boundary segregation (happening on top of the phase segregation). This needs to be kept in mind when discussing the phase boundary segregation in multiphase alloys, as it is the case of studies where the alloying composition exhibits more than 0.5 at. % of Nb and Cr for Ref. [41] and Mn and Cr for Ref. [42].

Using atom-probe-tomography (APT), Klein *et al.* [41] found Si to strongly partition into the  $\alpha_2$  bulk phase. Although our results suggest Si to segregate to the  $\alpha_2$  side of the interface, the energy gain at the interface itself is rather small  $|E_{\gamma \rightarrow \alpha_2}^f| \gg |E_{\alpha_2 \rightarrow \alpha_2/\gamma}^f|$ . Moreover, the segregation to the interface may be soon disadvantaged by a Si accumulation during the initial phase of the partitioning process, which will later lead to a substantial amount of Si in the  $\alpha_2$  grain due to  $E_{\gamma \rightarrow \alpha_2}^f \ll 0$ . Mn and Cr [42] and Mo [41] were also experimentally reported to partition into the  $\alpha_2$  phase, fully in line with our predictions.

Gerstl *et al.* [42,43] reported on a partitioning of Zr and Nb to the  $\gamma$  bulk phase. In our predictions, both of these elements would prefer to occupy sites at the  $\gamma$  side of the interface.

Using similar arguments as for Si above, we speculate that the segregation tendency of the  $\gamma$  side of the interface will be saturated and at later stages, which presumably correspond to the experimental conditions, Zr and Nb will occupy  $\gamma$  bulk site (which are preferred over any site in the  $\alpha_2$  phase). Especially for Y and Nb, the scales in Fig. 8 reveal a small difference between the  $\gamma$  bulk and  $\alpha_2/\gamma$  state.

Finally, let us recall the APT measurement of Gerstl *et al.* [42,43] proving that Hf favors the  $\alpha_2$  side of the  $\alpha_2/\gamma$  interface, fully in line with our results.

As for most elements, the phase preference ( $E_{\gamma \rightarrow \alpha_2}^f$ ) tends to overrule interface segregation, we especially want to highlight Nb, Hf, Zr, and Sc (where  $|E_{\gamma \rightarrow \alpha_2}^f|$  is small) as promising candidates for tailoring interface properties. Elements such as Mn, Fe, Co, Re, etc. will exhibit a strong thermodynamic force to partition into one phase, which inhibits any potential of using them for grain-boundary-based microstructure design. On the contrary, Nb, Hf, Zr, and Sc could be engineered to stay at the interface, since the phase preference may be overruled by thermal contributions.

In conclusion, although the specimens underwent heat treatments and show complex alloying concepts in the experimental studies [41–43] our predictions show very good qualitative predictive power. Some discrepancies may be related to the actual overall amount of the alloying element—our calculations correspond to a dilute limit—the overall alloy constitution—we assume ideal compositions of the  $\alpha_2$  and  $\gamma$  phases, and finite temperature heat treatments.

## V. CONCLUSIONS

We have extended and benchmarked a recently proposed quantum-mechanical/classical-mechanical coupling method in order to study site preference, and segregation to the  $\alpha_2(0001)/\gamma(111)$  Ti<sub>3</sub>Al/TiAl interface. Innovatively, we have applied the QM/MM method to a two-phase two-component system.

First, we have shown that our QM/MM method is capable of reproducing DFT results not only qualitatively but also quantitatively, by discussing the site preference for a series of substitutional solutes. Those were considered not only in

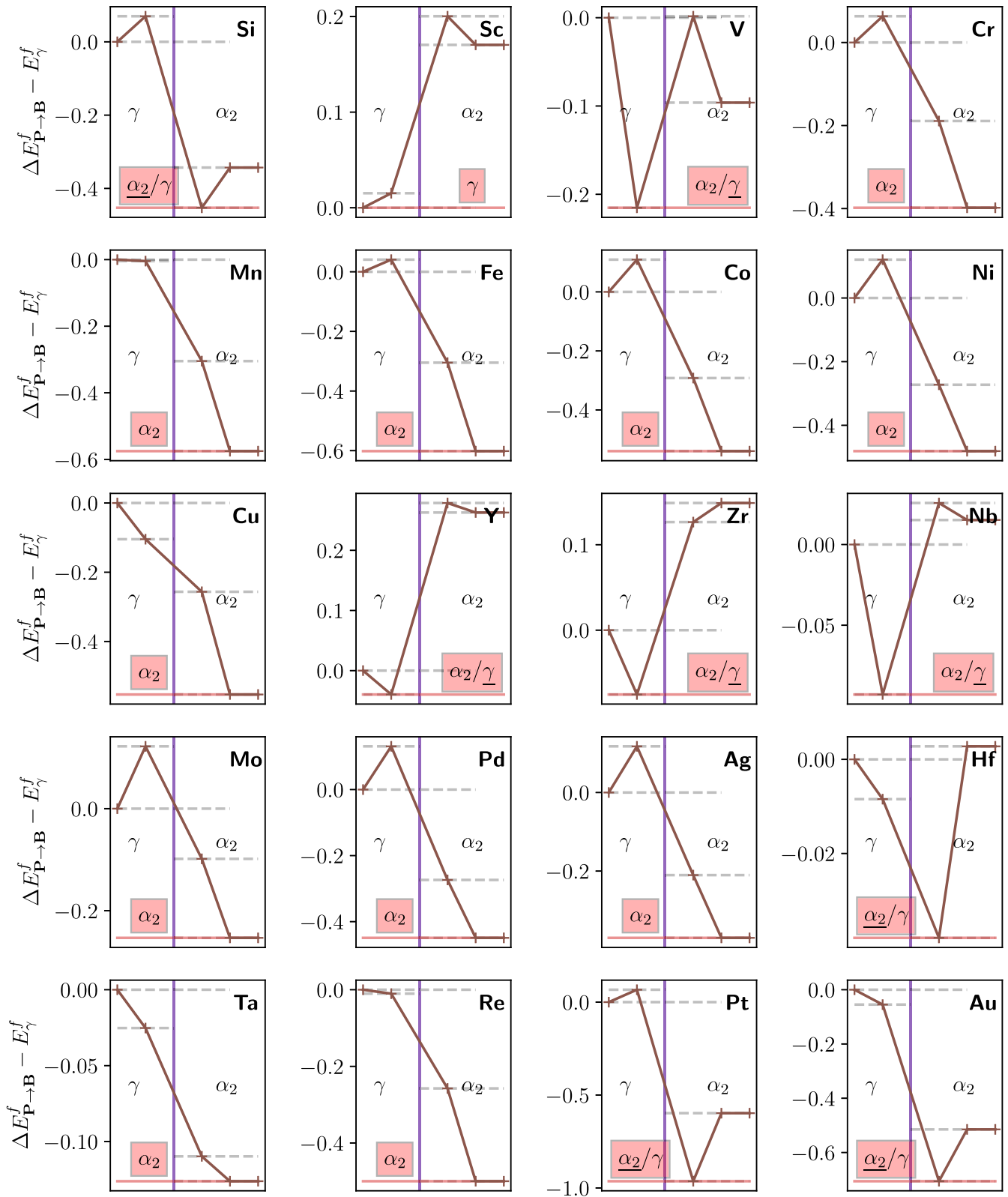


FIG. 8. Segregation energies [Eqs. (8)–(10)] are shown in reference to  $E_\gamma^f$ . The purple line represents the  $\alpha_2/\gamma$  interface. In each plot, the  $x$  axis represents the states of the solute in  $\gamma$  bulk (very left), at  $\alpha_2/\gamma$  (left of the purple line),  $\alpha_2/\gamma$  (right of the purple line), and in the  $\alpha_2$  bulk (very right). The brown line represents the energy difference with respect to  $E_\gamma^f$ .

the bulk phases but also at the interfaces. Our results suggest that in all the systems considered in this work, the interface site preference is mostly identical to that of the corresponding bulk phase.

Next, we have extensively studied segregation behavior at both interfaces. We have also considered the possibility, that the preferred sublattice changes from bulk to the interface, and hence possesses an additional barrier for solute segregation to the interfaces. While this is not the case for the investigated interfaces, it may be of importance for other interfaces and/or engineering alloys. Additionally, we identified solutes that tend to segregate to a  $\alpha_2/\gamma$  interface (e.g., Si, Hf, V, Y, Zr, Nb, or Pt), and those which tend to prefer bulk phases. Most importantly, decent agreement with experimental APT measurements for nearly all solutes was obtained.

Finally, we want to point out that, although not shown in the present work, the proposed QM/MM approach can be straightforwardly applied to more general interfaces and grain boundaries. As the method is not restricted to periodic boundary conditions, also low symmetry defects can be investigated, which are not tractable with DFT anymore.

#### ACKNOWLEDGMENTS

L.H. and J.N. are part of SFB1394 and gratefully acknowledge funding by the German Research Foundation [Deutsche Forschungsgemeinschaft (DE)], Project No. 409476157. D.G. greatly appreciates the support from the Austrian Academy of Sciences (DOC scholarship). D.H. appreciates financial support from the Austrian Science Fund (FWF) Project No. P29731-N36. The computational results were in part achieved by using the VSC computing infrastructure. D.G. sincerely appreciates the suggestions from Dr. M. Friák (IPM Brno, Czech Republic).

#### APPENDIX A: THERMODYNAMIC LIMITS OF THE DIFFERENCE OF THE CHEMICAL POTENTIALS

##### 1. For the $\alpha_2$ -bulk phase

The thermodynamic limits for the  $\alpha_2$  phase, which is bordered by the  $\alpha$ -Ti with  $\approx 6$  at. Al, and the  $\gamma$ -TiAl phase. As the  $\alpha$ -Ti with Al is a solid solution we have calculated the energy of five different optimized special quasirandom [44] (SQS) structures. Those (SQS) structures' pair-correlations were optimized by systematically probing all possible ( $25.6 \cdot 10^6$ ) atomic arrangements using the *sqsgenerator* package [45]. Each cell having 81 ( $3 \times 3 \times 3$ -supercell) atoms from which five were aluminum (6.17 at. Al). For  $\alpha$ -Ti and  $\alpha_2$ -Ti<sub>3</sub>Al to coexist we require

$$\frac{\bar{E}_{\text{SQS}}^\alpha}{9} = \frac{5}{81}\mu^{\text{Al}} + \frac{76}{81}\mu^{\text{Ti}}, \quad (\text{A1})$$

$$E^{\alpha_2} = 3\mu^{\text{Ti}} + \mu^{\text{Al}}. \quad (\text{A2})$$

Therefore we obtain the lower limit

$$\Delta\mu_{\alpha/\alpha_2} = \mu_{\alpha/\alpha_2}^{\text{Ti}} - \mu_{\alpha/\alpha_2}^{\text{Al}} = \frac{1}{61}(36E_\alpha - 81E_{\alpha_2}). \quad (\text{A3})$$

Similarly for the upper thermodynamic limit ( $\gamma$ -TiAl), from requiring

$$E^\gamma = \mu^{\text{Ti}} + \mu^{\text{Al}}, \quad (\text{A4})$$

$$E^{\alpha_2} = 3\mu^{\text{Ti}} + \mu^{\text{Al}}, \quad (\text{A5})$$

we get analogously

$$\Delta\mu_{\alpha_2/\gamma} = \mu_{\alpha_2/\gamma}^{\text{Ti}} - \mu_{\alpha_2/\gamma}^{\text{Al}} = E^{\alpha_2} - 2E^\gamma. \quad (\text{A6})$$

##### 2. For the $\gamma$ -bulk phase

The  $\gamma$ -TiAl phase is, for lower Al contents bordered by the  $\alpha_2$ -Ti<sub>3</sub>Al phase, is hence given by Eq. (A6). For higher aluminum contents the  $\gamma$ -phase field borders the  $h$ -TiAl<sub>2</sub>. Again, for both phases to coexist

$$E^h = \mu^{\text{Ti}} + 2\mu^{\text{Al}}, \quad (\text{A7})$$

$$E^\gamma = \mu^{\text{Ti}} + \mu^{\text{Al}}, \quad (\text{A8})$$

from which we obtain

$$\Delta\mu_{\gamma/h} = \mu_{\gamma/h}^{\text{Ti}} - \mu_{\gamma/h}^{\text{Al}} = 3E^\gamma - 2E^h. \quad (\text{A9})$$

#### APPENDIX B: BENCHMARK OF DEFECT FORMATION ENERGIES AT THE INTERFACE

Similarly to Fig. 5 for the bulk phases, Fig. 9 compares the formation energy for the solute point defects at the interface with DFT and Ref. [15]. Note that due to the coexistence of the  $\alpha_2$  and  $\gamma$  bulk phase, the thermodynamically allowed range collapses into a scalar. The upper and lower panels in Fig. 9 refer to the  $\alpha_2$  and  $\gamma$  sides of the interfaces, respectively.

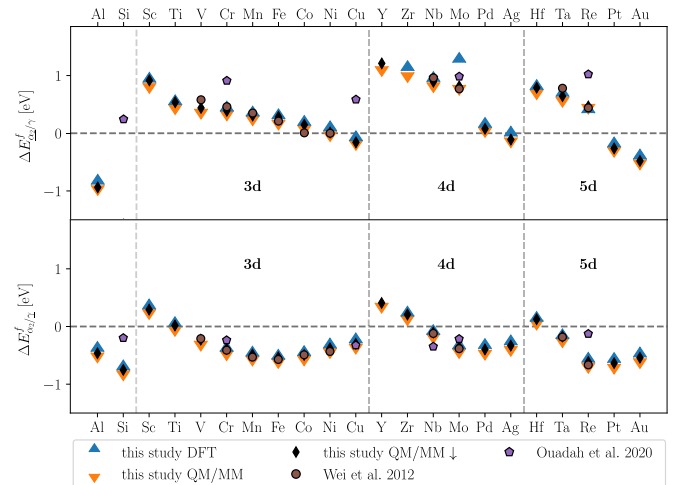


FIG. 9. Difference of the defect formation energy between the Ti and Al sublattice for  $\alpha_2/\gamma$  (upper panel) and  $\alpha_2/\gamma$  (lower panel) decorated interfaces. Points, representing literature data, exhibit a small black border.

APPENDIX C: QM/MM ALGORITHM FLOWCHART

Our implementation of the QM/MM algorithm builds on a workflow infrastructure implemented in pyiron. Therein, we employ directed graphs to control the execution. Fig. 10 shows how the coupling between QM and MM is implemented as a directed graph.

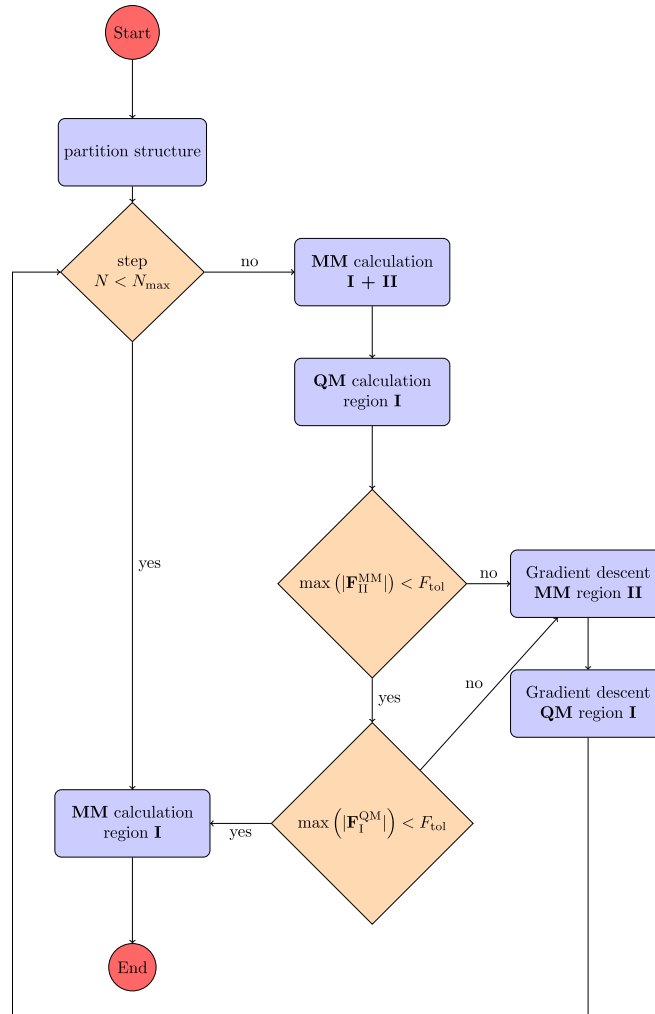


FIG. 10. Visualization of the execution flow of the employed QM/MM algorithm. Following the notation from previous works, **I** refers to the QM and **II** to the MM domain.

APPENDIX D: POINT DEFECT PHASE DIAGRAMS

The formation energy for a solute point defect in the bulk is a function of the difference chemical potentials of the host species  $\delta\mu_P$ . Therefore Fig. 11 shows this dependence for the  $\alpha_2$  and Fig. 12 for the  $\gamma$  bulk phase. The thermodynamic limits (blue and orange shaded regions) are derived in Appendix A.1 for Fig. 11 and Appendix A.2 for Fig. 12. In case the formation energy (red solid line) exhibits a sign change (intercept with the dashed black line) within the thermodynamic allowed range (white space) we refer to the solute as “weakly” preferring the respective sublattice.

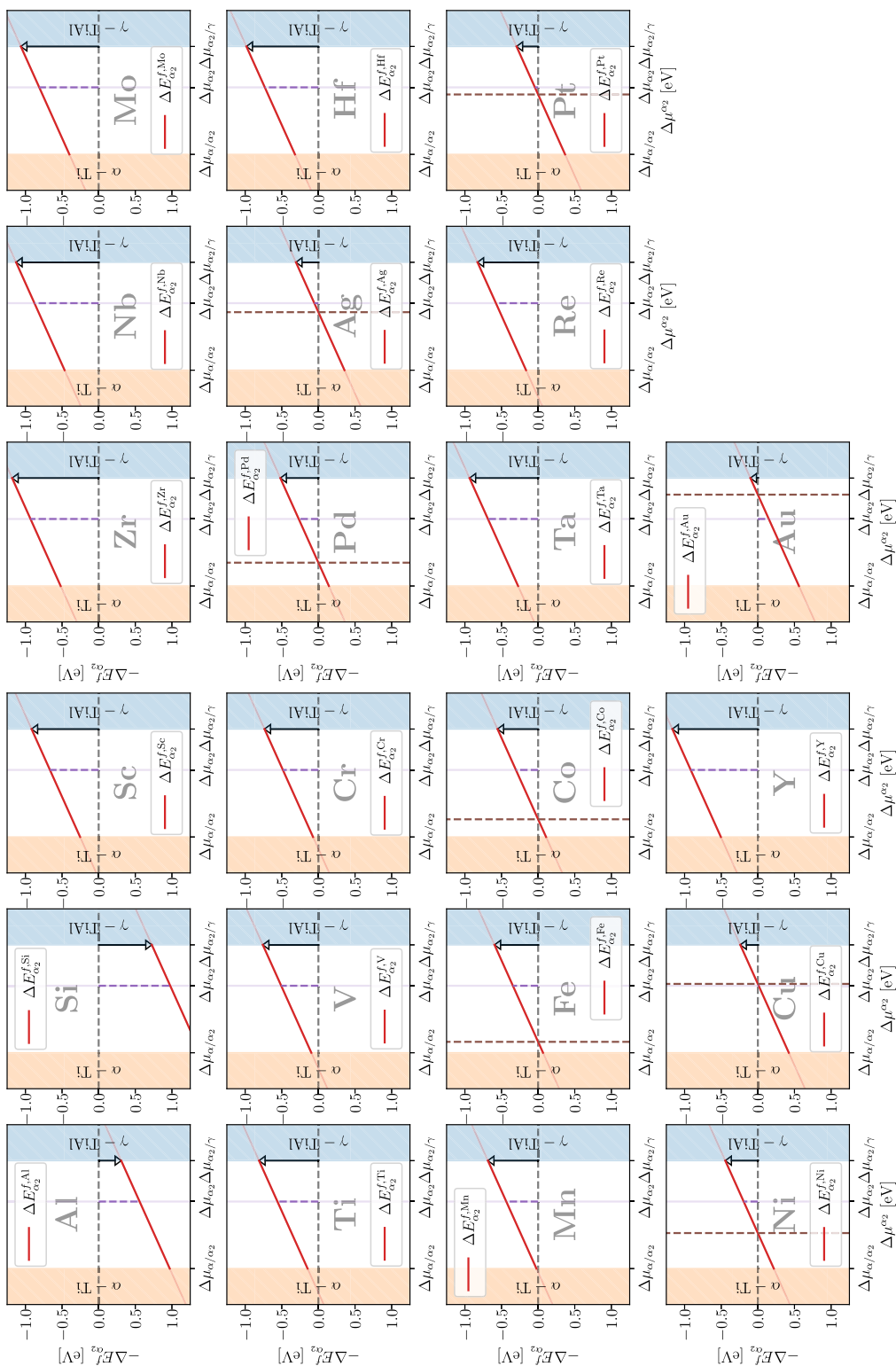


FIG. 11. Point defect phase diagram for different solutes in the  $\alpha_2$  phase. The x axis shows the  $\Delta\mu_{\alpha_2}$  as calculated in A.1.

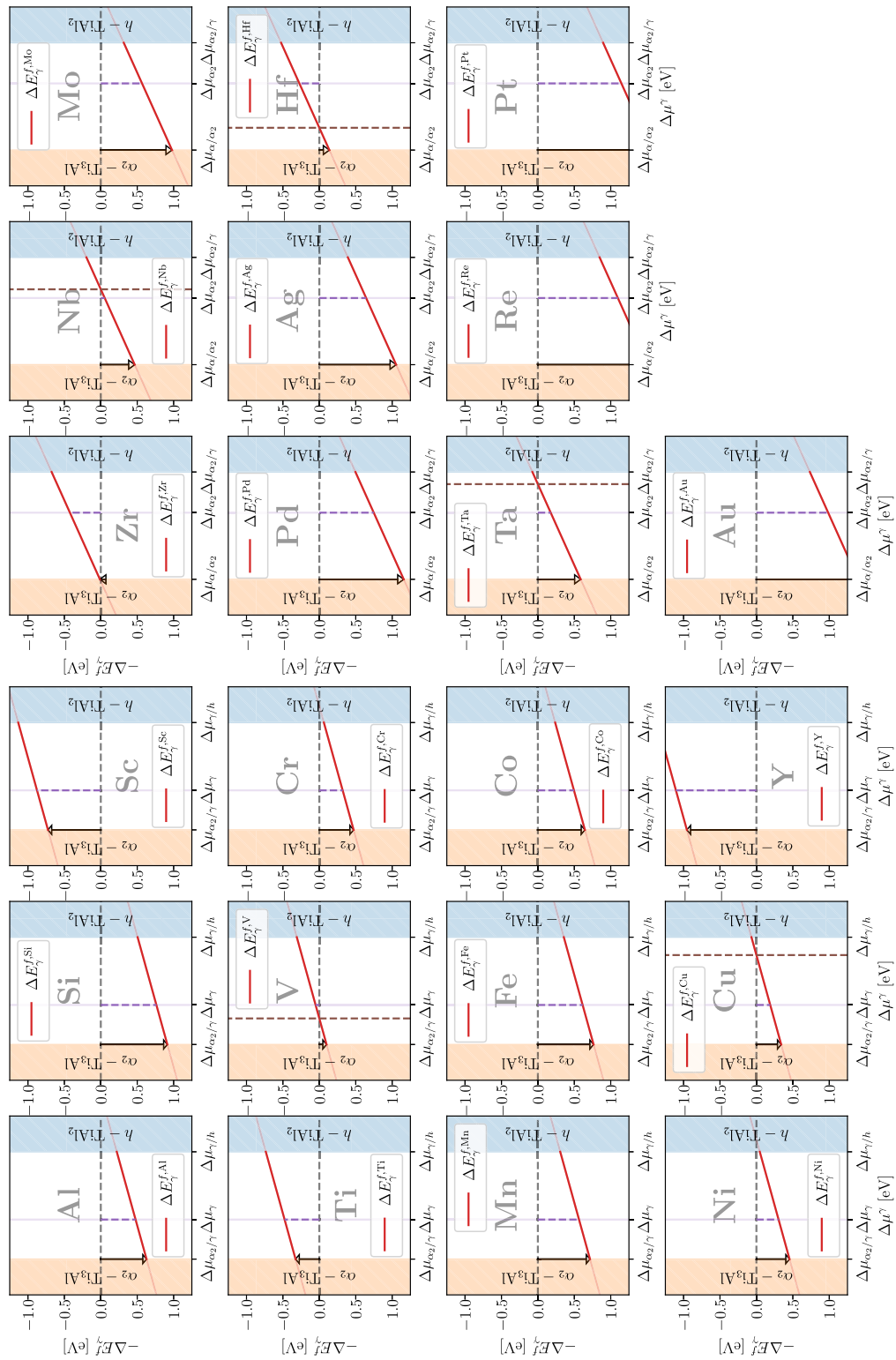


FIG. 12. Point defect phase diagram for different solutes in the  $\gamma$  phase. The x axis shows the  $\Delta\mu_\gamma$  as calculated in A 2.

[1] Y. Mishin, *Acta Mater.* **214**, 116980 (2021).

[2] I. S. Novikov, K. Gubaev, E. Podryabinkin, and A. V. Shapeev, *MLST 2*, 025002 (2020).

[3] P. Grigorev, A. M. Goryaeva, M.-C. Marinica, J. R. Kermode, and T. D. Swinburne, *Acta Mater.* **247**, 118734 (2023).

- [4] N. Choly, G. Lu, W. E. and E. Kaxiras, *Phys. Rev. B* **71**, 094101 (2005).
- [5] Y. Zhao, C. Wang, Q. Peng, and G. Lu, *Comput. Mater. Sci.* **50**, 714 (2010).
- [6] Y. Liu, G. Lu, Z. Chen, and N. Kioussis, *Modell. Simul. Mater. Sci. Eng.* **15**, 275 (2007).
- [7] X. Zhang, G. Lu, and W. A. Curtin, *Phys. Rev. B* **87**, 054113 (2013).
- [8] L. Huber, B. Grabowski, M. Militzer, J. Neugebauer, and J. Rottler, *Comput. Mater. Sci.* **118**, 259 (2016).
- [9] H. Clemens and S. Mayer, *Adv. Eng. Mater.* **15**, 191 (2012).
- [10] D. Holec, N. Abdoshahi, D. Gehringer, L. Hatzenbichler, A. Sakic, and H. Clemens, *Adv. Eng. Mater.* **24**, 2100977 (2021).
- [11] L. Huber, J. Rottler, and M. Militzer, *Acta Mater.* **80**, 194 (2014).
- [12] D. Scheiber, R. Pippin, P. Puschnig, A. Ruban, and L. Romaner, *IJRMHM* **60**, 75 (2016).
- [13] M. Kanani, A. Hartmaier, and R. Janisch, *Intermetallics* **54**, 154 (2014).
- [14] M. Kanani, A. Hartmaier, and R. Janisch, *Acta Mater.* **106**, 208 (2016).
- [15] Y. Wei, Y. Zhang, G.-H. Lu, and H. Xu, *Intermetallics* **31**, 105 (2012).
- [16] G. Kresse and J. Hafner, *Phys. Rev. B* **47**, 558 (1993).
- [17] G. Kresse and J. Furthmüller, *Phys. Rev. B* **54**, 11169 (1996).
- [18] J. P. Perdew, K. Burke, and M. Ernzerhof, *Phys. Rev. Lett.* **77**, 3865 (1996).
- [19] R. Elmer, M. Berg, L. Carlen, B. Jakobsson, B. Noren, A. Oskarsson, G. Ericsson, J. Julien, T. F. Thorsteinsen, M. Guttormsen, G. Lovhoiden, V. Bellini, E. Grosse, C. Muntz, P. Senger, and L. Westerberg, *Phys. Rev. Lett.* **78**, 1396(E) (1997).
- [20] P. E. Blöchl, *Phys. Rev. B* **50**, 17953 (1994).
- [21] G. Kresse and D. Joubert, *Phys. Rev. B* **59**, 1758 (1999).
- [22] H. J. Monkhorst and J. D. Pack, *Phys. Rev. B* **13**, 5188 (1976).
- [23] S. Plimpton, *J. Comput. Phys.* **117**, 1 (1995).
- [24] LAMMPS lammps molecular dynamics simulator, <https://lammps.sandia.gov>.
- [25] R. R. Zope and Y. Mishin, *Phys. Rev. B* **68**, 024102 (2003).
- [26] F. Bianchini, A. Glielmo, J. R. Kermode, and A. De Vita, *Phys. Rev. Mater.* **3**, 043605 (2019).
- [27] L. Huber, B. Grabowski, M. Militzer, J. Neugebauer, and J. Rottler, *Acta Mater.* **132**, 138 (2017).
- [28] pyiron development team, pyiron\_contrib, [https://github.com/pyiron/pyiron\\_contrib](https://github.com/pyiron/pyiron_contrib).
- [29] J. Janssen, S. Surendralal, Y. Lysogorskiy, M. Todorova, T. Hickel, R. Drautz, and J. Neugebauer, *Comput. Mater. Sci.* **163**, 24 (2019).
- [30] V. Witusiewicz, A. Bondar, U. Hecht, S. Rex, and T. Velikanova, *J. Alloys Compd.* **465**, 64 (2008).
- [31] D. Holec, R. K. Reddy, T. Klein, and H. Clemens, *J. Appl. Phys.* **119**, 205104 (2016).
- [32] R. Benedek, A. van de Walle, S. S. A. Gerstl, M. Asta, D. N. Seidman, and C. Woodward, *Phys. Rev. B* **71**, 094201 (2005).
- [33] O. Ouadah, G. Merad, and H. S. Abdelkader, *Mater. Chem. Phys.* **257**, 123434 (2021).
- [34] Yang Jinlong, Xiao Chuanyun, Xia Shangda, and Wang Kelin, *Phys. Rev. B* **46**, 13709 (1992).
- [35] H. Erschbaumer, R. Podloucky, P. Rogl, G. Temnitschka, and R. Wagner, *Intermetallics* **1**, 99 (1993).
- [36] W. Wolf, R. Podloucky, P. Rogl, and H. Erschbaumer, *Intermetallics* **4**, 201 (1996).
- [37] Y. Song, R. Yang, D. Li, Z. Hu, and Z. Guo, *Intermetallics* **8**, 563 (2000).
- [38] Y. Song, Z. Guo, and R. Yang, *J. Light Metal.* **2**, 115 (2002).
- [39] C. Jiang, *Acta Mater.* **56**, 6224 (2008).
- [40] Y. Hao, D. Xu, Y. Cui, R. Yang, and D. Li, *Acta Mater.* **47**, 1129 (1999).
- [41] T. Klein, B. Rashkova, D. Holec, H. Clemens, and S. Mayer, *Acta Mater.* **110**, 236 (2016).
- [42] S. S. Gerstl, Y.-W. Kim, and D. N. Seidman, *Interface Sci.* **12**, 303 (2004).
- [43] S. Gerstl, Y. Kim, and D. Seidman, *Microsc. Microanal.* **8**, 1096 (2002).
- [44] S. H. Wei, L. G. Ferreira, J. E. Bernard, and A. Zunger, *Phys. Rev. B* **42**, 9622 (1990).
- [45] D. Gehringer, M. Friák, and D. Holec, *Comput. Phys. Commun.* **286**, 108664 (2023).